Explicit modeling and optimization of acoustic meta-lenses for baffled sources

Théo Cavalieri,* Vicent Romero-García,† Manuel Melon, and Jean-Philippe Groby
Laboratoire d'Acoustique de l'Université du Mans (LAUM), UMR 6613, Institut d'Acoustique-Graduate School (IA-GS), CNRS, Le Mans Université, Avenue Olivier Messiaen, 72085 Le Mans, France

Jean-Christophe Chamard
Stellantis, Centre Technique Vélizy, Route de Gisy, 78943 Vélizy-Villacoublay Cedex, France

(Dated: June 23, 2023)

The steering and the focusing of acoustic beams are of increasing interest for personalized sound zone applications. Sound zones require to generate a strong contrast in sound pressure level (SPL) between different regions of the space. A way to do so is to control and steer the acoustic field radiated from a source using metamaterial-based acoustic lenses. To date, predictive models based on numerical approaches such as the finite-elements method (FEM) are commonly used, but are generally cumbersome and time-consuming. In the opposite, explicit models rely on Snell's law of refraction and phase gratings, but do not account for the couplings between the metamaterial atoms. In this work, a metamaterial-based acoustic lens is proposed as a solution to steer and focus acoustic sources, using slits loaded by periodic Helmholtz resonators. We control the radiation of a baffled duct by a meta-lens located at the output of the waveguide and excited at the other end by a loudspeaker. A fully explicit two-dimensional predictive model is developed based on mode-matching technique, accounting for thermo-viscous losses, inter-slit evanescent coupling, and high-order modes in the baffled duct. The pressure radiated by the meta-lens outside of the baffled duct is then explicitly derived. The semi-analytical results show excellent agreement when compared to the solutions obtained by FEM, both in the near- and far-field over a wide frequency range. An optimization strategy is then proposed and the beam steering and focusing are reported experimentally on a 3D-printed prototype.

Keywords: meta-materials; acoustic lens; explicit modeling; finite elements; directivity control

I. INTRODUCTION

Recently, the possibility to create and control acoustic sound-zones has been of growing interest [5, 12, 23**?**]. Sound zones require to create a contrast in sound pressure level (SPL) between distinct regions of the space. Such applications have already been addressed using active (electro-mechano-acoustic) solutions [5, 33], but passive acoustic structures can also establish high SPL contrast by confining acoustic energy in some regions of space, while maintaining low amplitudes in other regions. Acoustic lenses are of interest in this latter case. While active solutions require additional sources of electrical power, passive solutions are purely based on a structured treatment and require no additional sources of energy. Both the growing prospective applications of acoustic meta-materials and the elementary nature of passive acoustic lenses initiate the need of modeling tools. Numerical simulations are generally more suitable than analytical models at solving complex problems, but are often accompanied by high computational costs. However, a well-designed analytical model can provide accurate results in a short amount of time. This is especially efficient for the rapid optimization and design of acoustic solutions and treatments.

In most of the scientific literature, acoustic lenses are modeled either numerically or explicitly by making use of phase arrays [21, 22]. Snell's law of refraction is valid when the phase gradient is continuous, i.e., the propagation medium itself has no discontinuities. However, the assumption of a continuous gradient of phase has to be questioned in the case of discrete structures, which are particularly common in the field of meta-materials [1, 2]. The motivation of this work is to propose a complete explicit model for meta-material-based acoustic lenses, which is not relying on phase gradients but rather on a 'mode-matching' approach [11]. This method also has the advantage of accounting for the couplings between the meta-material and its host waveguide, as preliminary studies to this work evidenced the need to account for high-order modes and inter-slits couplings in order to accurately predict the acoustic radiation

* Now at: EMPA, Swiss Federal Laboratories for Materials Science and Research, Überlandstrasse 129, 8600 Dübendorf, Switzerland; Correspondence: theo.cavalieri[at]empa.ch – tcaval[at]univ-lemans.fr
† Now at: Instituto Universitario de Matemática Pura y Aplicada (IUMPA), Universitat Politècnica de València, Camino de Vera s/n, 46022 València, Spain

of the meta-lens. A validation study is available in the Supplementary Material [36] of this paper, proving the capability of the explicit model to accurately predict the acoustic behavior of meta-lenses when compared to FEM results.

In this work, an array of slits loaded by Helmholtz resonators constitutes the meta-lens. Such a geometry offers a lot of flexibility as all the dimensions of both the slits and the resonators can be independently tuned. An optimization procedure is proposed in order to steer the acoustic beam at the outlet of the baffled duct. The optimization relies on the explicit expressions and uses model order reduction (MOR) techniques [3] and the particle swarm optimization (PSO) algorithm [19, 26]. The width of the slits and the geometry of the resonators are continuously graded according to a polynomial description and meant to provide acoustic beam-steering at a specific angle. The meta-lens with optimal geometry is then fabricated by additive manufacturing processes [10, 14] and tested experimentally in an anechoic chamber. This work paves the way of a complete analytical tool for the optimization of the radiation of acoustic lenses using meta-materials. Furthermore, the architecture of the present predictive model can be extended to design 3D meta-materials.

This article is organized as follows: First the principles of Snell's law of refraction and phase arrays are recalled in Sec. II. Then, the geometry of the meta-lens and the problem of acoustic wave propagation and radiation is presented in Sec. III, for which explicit and numerical solutions are proposed in Sec. IV. The meta-lens is optimized for a beam-steering configuration as detailed in Sec. V. This optimal configuration is then studied experimentally in Sec. VI and all the results are finally presented in Sec. VII. The conclusions, limitations, and perspectives of this work are discussed in Sec. VIII. The authors also invite the reader to dive into the Supplementary Material for a more detailed description of the underlying Physics and Mathematics on which this work is based.

II. REFRACTION-BASED ACOUSTIC LENSES

Introduced independently by Snell and Descartes in the 17th century, the refraction law states on the relationship between the angles of the incident and the refracted waves at the interface between two media [7]. It is now well established in the literature that it is possible to deviate –steer– an acoustic wave using a gradient of phase. This is achieveable by making use of heterogeneous media having space-dependent sound speed [21]. Consider a medium bounded by two interfaces Γ_0 and Γ_L with a graded phase $\Phi(x_1)$ along its vertical direction $\mathbf{e}_1$, as shown in Fig. 1. The generalized Snell's law gives the relation between both the incident and refracted angles [35] at the position x_1 as

$$\sin(\theta_\mathrm{t}(x_1)) = \frac{1}{k_0}\frac{\mathrm{d}\Phi}{\mathrm{d}x_1} + \sin(\theta_\mathrm{i}(x_1)) \ , \tag{II.1}$$

where $\theta_\mathrm{t}(x_1)$ and $\theta_\mathrm{i}(x_1)$ are the angles of refraction and incidence respectively, $k_0 = \omega/c_0$ is the wavenumber of the surrounding medium, with $\omega = 2\pi f$ the angular frequency and c_0 the sound speed in free field.

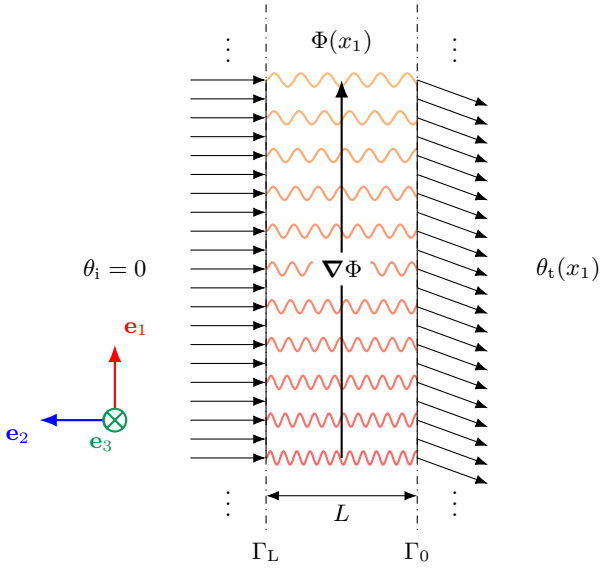

FIG. 1. (Color online) Conceptual representation of Snell's law where a layer is bounded by two interfaces Γ_0 and Γ_L with a graded phase $\phi(x_1)$ along its vertical direction $\mathbf{e}_1$. The incident and refracted angles are shown on either side of the layer by black arrows.

Considering a normal plane wave, i.e., $\theta_\mathrm{i} = 0$, and the phase function $\Phi(x_1) = \omega L/c(x_1)$, we end with

$$\sin(\theta_\mathrm{t}(x_1)) = Lc_0 \frac{\mathrm{d}}{\mathrm{d}x_1}\left(\frac{1}{c(x_1)}\right) , \tag{II.2}$$

where L is the thickness of the layer. Hence, the properties of the heterogeneous layer can be tuned in order to grade the phase at Γ_0. Different types of sound speed profiles can be designed depending on the desired effect [21].

III. SLITS & HELMHOLTZ RESONATORS AS ACOUSTIC META-LENSES

The acoustic propagation problem is set in the 2D Cartesian coordinate system with unit-vectors $\mathbf{e}_i$ and the position vector given by $\mathbf{x} = (x_1, x_2) \in \mathbb{R}^2$ as sketched in Fig. 2. First, a semi-infinite waveguide of height $w^{(0)}$ is considered and represented by the domain $\Omega^{(0)}$. Then, the meta-lens made of slits and Helmholtz resonators is positioned at one end of the main waveguide and represented by the domain Ω_π. The interface between the main waveguide $\Omega^{(0)}$ and the meta-lens Ω_π located at $x_2 = L$ is denoted Γ_L. The meta-lens itself is composed of N parallel slits denoted by the domains $\Omega_\mathrm{S}^{(n)}$, and $d^{(n)}$ and $w^{(n)}$ are respectively the lowest position and the width of the n-th slit along the direction $\mathbf{e}_1$, see the inset in Fig. 2.

The set of slits is introduced by $\mathcal{N} = \{1, \ldots, N\} \subset \mathbb{N}^\star$. The duct and the meta-lens are baffled at $x = 0$ and radiate in a semi-infinite half-space shown as a semicircle on the right-hand side of Fig. 2. The half-space is connected to the other end of the slits is simply denoted by the domain $\Omega^{(\mathrm{rad})}$.

The interface between the slits and the half-space at $x_2 = 0$ is Γ_0. Both interfaces respectively contain $\Gamma_\mathrm{L}^{(n)}$ and $\Gamma_0^{(n)}$, to make the distinction between the open and closed boundaries at both ends of the meta-material, as detailed in Eq. (III.1). Finally, each slit is loaded by Q identical and evenly spaced Helmholtz resonators (with spacing b_uc), the Helmholtz resonators may differ from one slit to another. A slit loaded by Helmholtz resonators is shown in Fig. 3. The wave propagation in the slits $\Omega_\mathrm{S}^{(n)}$ is governed by the geometric features of the resonant periodic structure. Consider $\mathcal{Q} = \{1, \ldots, Q\} \subset \mathbb{N}^\star$ the set of Helmholtz resonators in parallel of the n-th slit. The q-th resonator is made of a neck $\Omega_{\mathrm{N},q}^{(n)}$ and a cavity $\Omega_{\mathrm{C},q}^{(n)}$. Thus, each resonator is defined by the domain $\Omega_{\mathrm{H},q}^{(n)}$. Moreover, the portions of the slits before and after the resonators are denoted $\Omega_{\mathrm{S},+}^{(n)}$ and $\Omega_{\mathrm{S},-}^{(n)}$ respectively, and are shown in light orange on Fig. 3. These sub-slits have length $b_+^{(n)}$ and $b_-^{(n)}$. Albeit, the dimensions of the entire slits satisfy $L \coloneqq b_+^{(n)} + (Q-1)b_\mathrm{uc} + b_-^{(n)}$. In a more formal way, the domains that describe the geometry of the system satisfy

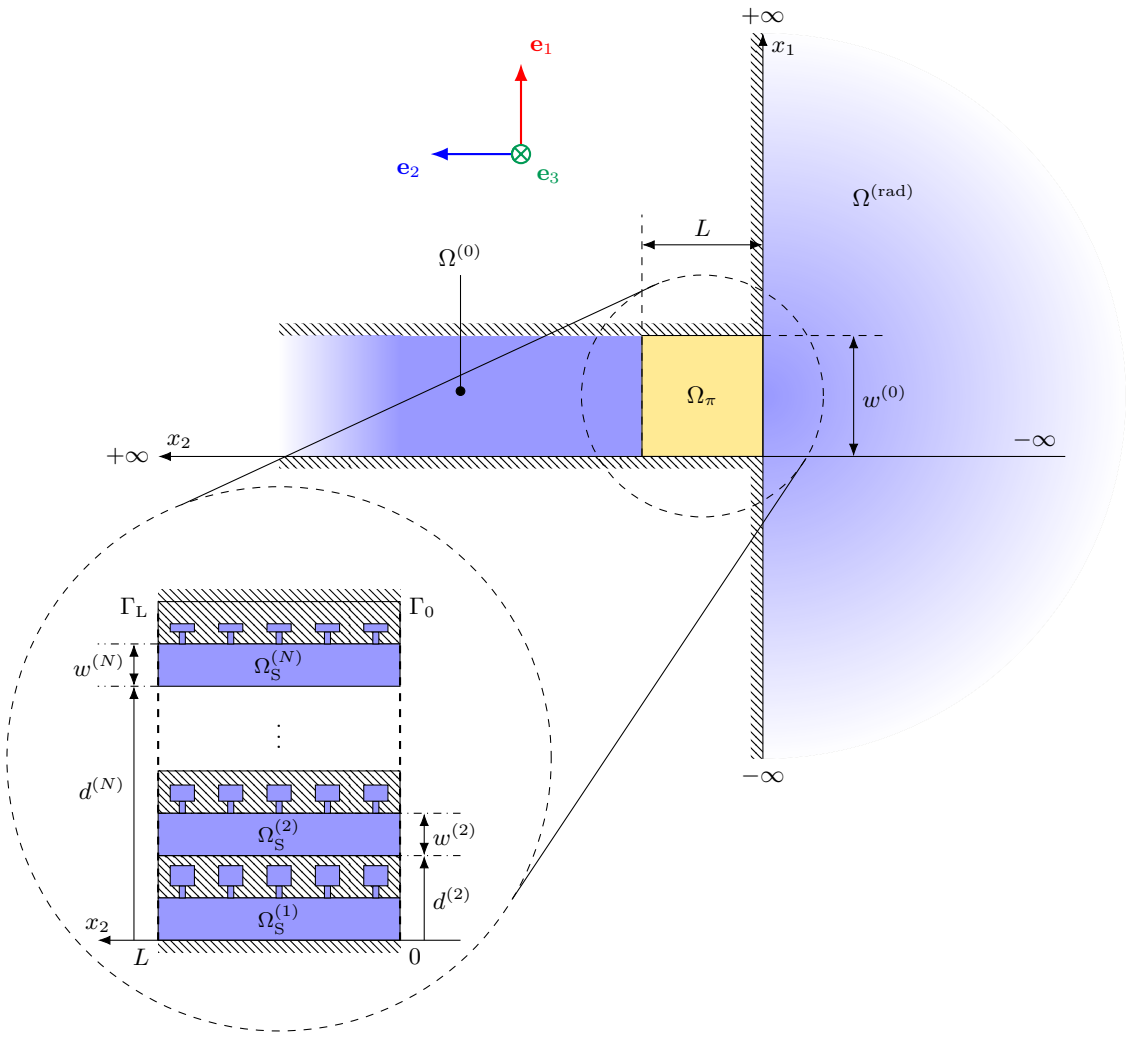

FIG. 2. (Color online) Sketch of the 2D system, the waveguide $\Omega^{(0)}$ and exterior domain $\Omega^{(\mathrm{rad})}$ are in shaded blue, and the resonant meta-lens Ω_π is shown in yellow. Under the magnifying glass is a sketch of the slits and periodic resonators within the meta-lens Ω_π.

$$\begin{cases} \Omega^{(0)} &= \left\{\mathbf{x}\in\mathbb{R}^2 \mid x_2 \geq L\ ,\ x_1 \in \left[0, w^{(0)}\right]\right\}\ , \\ \Omega_\mathrm{S}^{(n)} &= \left\{\mathbf{x}\in\mathbb{R}^2 \mid x_2 \in [0,L]\ , x_1 \in [d^{(n)}, d^{(n)}+w^{(n)}]\right\}\ , \\ \Omega^{(\mathrm{rad})} &= \left\{\mathbf{x}\in\mathbb{R}^2 \mid x_2 \leq 0\right\}\ , \\ \Omega_{\mathrm{H},q}^{(n)} &= \Omega_{\mathrm{N},q}^{(n)} \cup \Omega_{\mathrm{C},q}^{(n)}\ , \end{cases} \tag{III.1}$$

and the interfaces are given by

$$\begin{cases} \Gamma_\mathrm{L} &= \Omega^{(0)} \cap \Omega_\pi\ , \\ \Gamma_0 &= \Omega^{(\mathrm{rad})} \cap \Omega_\pi\ , \\ \Gamma_\mathrm{L}^{(n)} &= \Omega^{(0)} \cap \Omega_\mathrm{S}^{(n)}\ , \\ \Gamma_0^{(n)} &= \Omega^{(\mathrm{rad})} \cap \Omega_\mathrm{S}^{(n)}\ . \end{cases} \tag{III.2}$$

IV. EXPLICIT & NUMERICAL MODELING

In this section, two different modeling approaches are presented. The first one constitutes the analytical model and uses modal projection in order to obtain the pressure and velocity at the end of each slit, while FEM is used as a validation of the aforementioned analytical model. Extensive details are provided in the Supplementary Material.

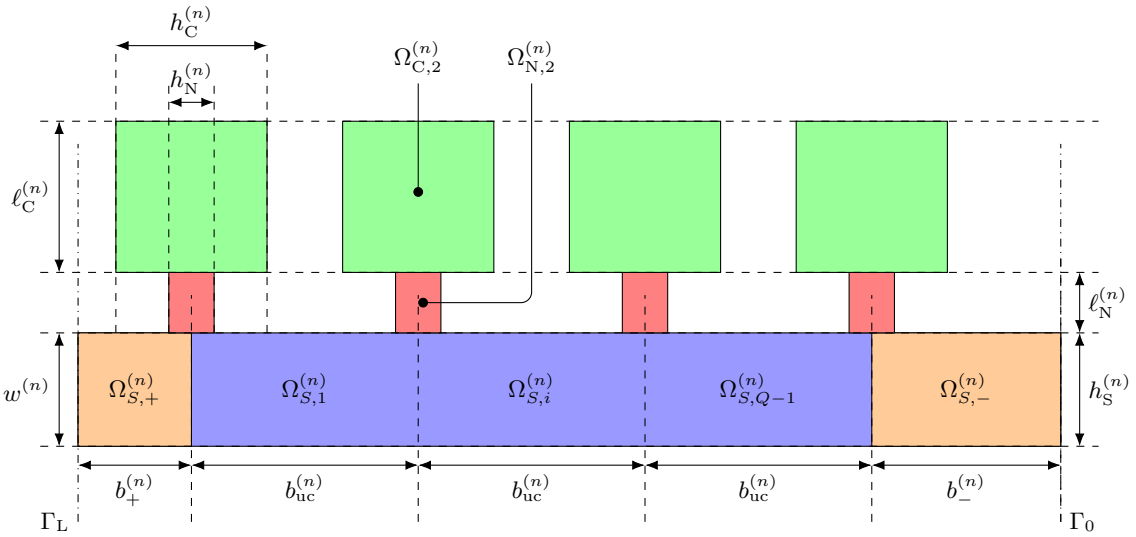

FIG. 3. (Color online) Sketch of the Helmholtz resonators mounted onto a single slit. The slit $\Omega_{\mathrm{S}}^{(n)}$ is shown in blue, its start and end sub-slits in orange, the cavities in green, and the necks in red.

A. Mode-matching techniques

Acoustic wave propagation under normal temperature and pressure is assumed, in the linear domain with Fourier time convention $\mathrm{e}^{-\mathrm{i}\omega t}$. Thus, the time dependence of the acoustic fields is omitted in the following statements. An incident plane wave in the main duct $\Omega^{(0)}$ propagating along the direction $-\mathbf{e}_2$ is considered. The pressure field is denoted p and the particle velocity vector is $\mathbf{v} = (v_1, v_2)$. The pressure field in the domain $\Omega^{(0)}$ is given by the infinite sum of all modal components along $\mathbf{e}_1$ and the general Green's formulation is employed in the half-space $\Omega^{(\mathrm{rad})}$:

$$p^{(0)}(\mathbf{x},\omega) = \sum_{m\in\mathbb{N}} \cos\left(k_{1,m}^{(0)} x_1\right)\left[\delta_m \mathrm{e}^{-\mathrm{i}k_{2,m}^{(0)}(x_2-L)} + R_m \mathrm{e}^{\mathrm{i}k_{2,m}^{(0)}(x_2-L)}\right] , \tag{IV.1a}$$

$$p^{(\mathrm{rad})}(\mathbf{x},\omega) = \int_{-\infty}^{+\infty} T^{(\mathrm{rad})}\left(k_1^{(\mathrm{rad})},\omega\right)\left[\mathrm{e}^{\mathrm{i}k_1^{(\mathrm{rad})}x_1 - \mathrm{i}k_2^{(\mathrm{rad})}x_2}\right]\frac{\mathrm{d}k_1^{(\mathrm{rad})}}{k_2^{(\mathrm{rad})}} , \tag{IV.1b}$$

with δ_m the Kronecker delta ($\delta_0 = 1$ defines the incident plane wave), and the wavevectors satisfy

$$\mathbf{k}_m^{(0)} = \left(\frac{m\pi}{w^{(0)}} , \sqrt{\left(k^{(0)}\right)^2 - \left(\frac{m\pi}{w^{(0)}}\right)^2}\right)^{\top} , \tag{IV.2a}$$

$$k_2^{(\mathrm{rad})} = \left(\left(k^{(\mathrm{rad})}\right)^2 - \left(k_1^{(\mathrm{rad})}\right)^2\right)^{1/2} , \tag{IV.2b}$$

such that their real part satisfies $\mathrm{Re}\left(k_{2,m}^{(0)}\right) \geq 0$, and $\mathrm{Re}\left(k^{(\mathrm{rad})}\right) \geq 0$. The superscript $\top$ denotes the non-conjugated transposition. In Eq. (IV.1a), the term R_m represents the reflection coefficient of the m-th mode of the duct at the interface Γ_{L}. Within each slit $\Omega_{\mathrm{S}}^{(n)}$ only the propagation of plane waves is assumed since their dimension along $\mathbf{e}_1$ is considered much smaller than the half-wavelength at the maximum frequency of interest. The pressure and normal velocity at both ends are thus linked by the corresponding transfer matrix [8, 18, 25, 27, 32]

$$\begin{pmatrix} p^{(n)} \\ \tilde{v}_2^{(n)} \end{pmatrix}_L = \mathbf{T}^{(n)} \begin{pmatrix} p^{(n)} \\ \tilde{v}_2^{(n)} \end{pmatrix}_0 . \tag{IV.3}$$

Here, the volume flow $\tilde{v}_2^{(n)} = S^{(n)}[\mathbf{e}_2 \cdot \mathbf{v}^{(n)}]$ is considered, with $S^{(n)}$ the cross-sectional area of each slit ($S^{(n)} = w^{(n)}$ in two dimensions). The matrix $\mathbf{T}^{(n)} \in \mathbb{C}^{2\times 2}$ is the transfer matrix that connects the state vectors at both interfaces and accounts for thermal and viscous losses within the slits and resonators, as well as the radiation corrections at

the discontinuities in the resonator and between the resonator and the slit [20, 31]. At both interfaces Γ_{L} and Γ_0 the continuity of the acoustic pressure and normal velocity is assumed and satisfies $\forall n \in \mathcal{N}$

$$\left\{\begin{array}{ll} p^{(0)} = p_{\mathrm{L}}^{(n)} & \forall x_1 \in \Gamma_{\mathrm{L}}^{(n)} \ , \\ v_2^{(0)} = v_2^{(n)} & \forall x_1 \in \Gamma_{\mathrm{L}}^{(n)} \ , \\ v_2^{(0)} = 0 & \forall x_1 \in \Gamma_{\mathrm{L}} \setminus \Gamma_{\mathrm{L}}^{(n)} \ , \end{array}\right. \qquad \left\{\begin{array}{ll} p^{(\mathrm{rad})} = p_0^{(n)} & \forall x_1 \in \Gamma_0^{(n)} \ , \\ v_2^{(\mathrm{rad})} = v_2^{(n)} & \forall x_1 \in \Gamma_0^{(n)} \ , \\ v_2^{(\mathrm{rad})} = 0 & \forall x_1 \in \Gamma_0 \setminus \Gamma_0^{(n)} \ . \end{array}\right. \tag{IV.4}$$

As the transfer matrix method (TMM) is only applicable for plane waves in the slits, the acoustic pressure field is assumed to be constant constant along x_1 on $\Gamma_0^{(n)}$ and $\Gamma_{\mathrm{L}}^{(n)}$ such as

$$\left\{\begin{array}{rcl} p_L^{(n)} w^{(n)} & = & \displaystyle\int_{\Gamma_{\mathrm{L}}^{(n)}} p^{(n)} \, \mathrm{d}x_1 \ , \\ p_0^{(n)} w^{(n)} & = & \displaystyle\int_{\Gamma_0^{(n)}} p^{(n)} \, \mathrm{d}x_1 \ . \end{array}\right. \tag{IV.5}$$

The continuity equations for acoustic pressure and particle velocity at both interfaces are projected onto the modes of the main duct, the plane mode of the slits, and on the Green's integral formulation for radiation in the half-space. After matching the modal amplitudes and making use of the TMM, a system of coupled linear equations is reached and cast into the form $\mathbf{H}\mathbf{b} = \mathbf{s}$ with $\mathbf{H}$ a matrix of size $2N \times 2N$. Inverting the system provides the pressures and particle velocities at the end of each slit as a unique solution to the vector of unknowns

$$\mathbf{b} = \left(p_0^{(1)} \ , \ \dots \ , \ p_0^{(N)} \ , \ v_2^{(1)}|_0 \ , \ \dots \ , \ v_2^{(N)}|_0 \right)^\top \ . \tag{IV.6}$$

The complete analytical model runs as follows: once the geometry is set, the losses within each sub-domain of Ω_π are computed, and then TMM is carried out. Finally the matrix $\mathbf{H}$ is built and inversed.

B. Numerical validation with FEM

In order to first validate the results of the explicit model, finite-element simulations of the acoustic propagation problem are performed. The simulations are carried-out using the software COMSOL Multiphysics®. The geometry presented in Sec. III is implemented and an incident plane wave is imposed in the main duct $\Omega^{(0)}$. In order to satisfy the Sommerfeld radiation condition [29, 30] for $x_2 < 0$, perfectly matched layers (PMLs) are implemented [4] and surround the half-space $\Omega^{(\mathrm{rad})}$. Neumann boundary conditions are applied to all boundaries of the meta-lens and to these of the baffled duct. The acoustic thermal and viscous dissipation in Ω_π is accounted for using effective complex and frequency-dependent wavenumber and characteristic impedance [31]. The mesh of the finite-element model is adapted to be finer in narrow regions, i.e., mainly in the resonators and around the interfaces Γ_{L} and Γ_0. The simulation is performed using at least 10 elements per wavelength. The FEM solution provides the acoustic pressure and particle velocity fields at all points in the main duct, in the meta-lens, and in the half-space.

For a meta-lens comprising $N = 10$ slits each loaded by $Q = 5$ resonators, the analytical model solves the problem for $N_{\mathrm{f}} = 100$ frequencies in 142 seconds, while the same problem in FEM takes around 200 seconds on a common laptop (MacBook Pro 13-inch, 2017, macOS 10.13.6, Intel Core i7 @2.5 GHz, RAM 16 GB @2133 MHz) running on MATLAB®. However, the performances of both models can differ a lot depending on the number of slits, the truncation of sums and integrals, the FEM mesh refinement, and so on. Although the time difference presented here does not appear to be significant, it becomes predominant for optimization over short frequency bands, particularly because of the meshing time with FEM. Finally, as the systems of equations are independent for each frequency, the whole process could be easily done with parallel computing.

C. Acoustic radiation

On the one hand, the far-field acoustic radiation of the system is obtained from the spatial Fourier transform of the acoustic normal velocity $v_2^{(0)}$ at the end of the slits, i.e., at the interface Γ_0. The far-field directivity function $D(\theta)$ is introduced as

$$D(\theta) = -\mathrm{i}\frac{\rho\omega^2}{2\pi} \int_{\Gamma_0} [\mathbf{e}_2 \cdot \mathbf{v}(x_1)] \, \mathrm{e}^{-\mathrm{i}k_0 \sin(\theta) x_1} \, \mathrm{d}x_1 \ , \tag{IV.7}$$

with $x_1 \in \Gamma_0$ and the far-field radiated pressure is $p^{(\mathrm{far})}(r,\theta) = (1/r)\mathrm{e}^{\mathrm{i}k_0 r}D(\theta)$ [34]. Here, θ denotes the angle from $\mathbf{e}_2$ to $\mathbf{e}_1$ and the distance from the origin is $r = |\mathbf{x}|$.

On the other hand, the near-field radiated acoustic pressure is calculated from the integral formulation given in Eq. (IV.1b), which has infinite bounds and singularities of the denominator have to be excluded. Using properties of symmetry and changes of variables, it is possible to solve for the radiated pressure $p^{(\mathrm{rad})}$ with a good accuracy. A complete validation study is proposed in the Supplementary Material over different test-cases. Both analytical and FEM results are in excellent agreement as long as the waves propagating in the slits are in the plane-wave regime. The numerical errors essentially come from the truncation of the high-order modes and radiation integrals, as well as additional couplings within the resonators which are not accounted for. More details are also given regarding the derivation of the directivity function, the near-field radiation integrals, as well as the transmission loss of the system.

V. OPTIMIZATION OF THE META-LENS

In order to control the far-field directivity of the meta-lens, its inner geometry is to be adapted. Thus, the analytical model serves as a kernel in an optimization problem. This leads to optimizing all possible individual parameters of the slits and of the resonators. Here, the commonly-used downhill simplex method (also known as the Nelder-Mead algorithm [24]) is unpractical because of the high number of parameters to optimize. In order to tackle this problem and to provide a fast and efficient minimization procedure, the number of parameters is reduced using polynomial interpolation and a proper minimization method is chosen.

A. Cost function & minimization strategy

It is common for some optimization procedures to define a cost function which is to be minimized, resulting in refining the parameters of the system at each iteration. Probably the most convenient and intuitive in the actual context, is to specify a shifted Gaussian curve as the objective far-field directivity D_{obj}. Thus, the objective function is defined as a lobe with

$$D^{\mathrm{obj}}(\theta) = \exp\left[-\frac{(\theta-\theta_{\mathrm{obj}})^2}{2\sigma^2}\right], \tag{V.1}$$

where $\theta_{\mathrm{obj}} \in [-\pi/2, \pi/2]$ is the angle where the directivity function is maximal and σ controls the width of the main lobe.

The cost function is defined as the quadratic error between D and the shifted Gaussian lobe D^{obj}, and is designed to inflict a strong penalty over the angle of maximal radiated pressure. This ensures the quadratic error is minimized while the steering angle $\theta_{\max} = \theta_{\mathrm{obj}}$ is reached. The cost function is cast into the form

$$J \coloneqq |\theta_{\max} - \theta_{\mathrm{obj}}| + \frac{1}{N_\theta}\sum_{i=1}^{N_\theta} |D_i - D_i^{\mathrm{obj}}|^2 , \tag{V.2}$$

with $N_\theta = 181$ the number of distinct angles between $-90°$ and $+90°$. A well-suited minimization routine for this problem is the particle swarm optimization (PSO) [19, 26]. The PSO converges towards a minimum of J relying on a herd of particles, at the position of which the cost function is evaluated. At each iteration, the position of each particle is updated based on its previous steps and on the lowest values of J encountered by the herd in the search-space. Such an optimization is computationally heavy because computing J for each iteration is based on the explicit model, having a large number of function evaluations is not a burden. In the present case, the optimization is initialized with ten particles distributed in every dimension of the search space as adding particles strengthens the method ability to converge towards the global minimum.

B. Model order reduction using polynomials

Although having a high number of dimensions can be tackled using PSO, an additional technique is implemented in order to reduce the number of parameters (and computation time) while maintaining flexibility in the search-space. This is provided by the $\mathcal{C}^1$-continuous piecewise cubic Hermite interpolating polynomials (PCHIP), which preserves

the monotonicity of the interpolated data [13]. Another approach would be the use of Bezier curves as they provide additional degrees of freedom and flexibility, but this is out of the scope of this work. For example: instead of optimizing the cavity length of the resonators independently across 10 slits, only the values at slits 1, 5, and 10 are actually optimized, while the cavity lengths for the other slits are interpolated using PCHIP. Thus, we can adjust the number of nodes for which the optimization is performed, as it impacts the possible geometric outcomes. The first node is at position $x_1 = 0$ and the last node is at position $x_1 = w^{(0)}$. Between them, the other nodes are placed at $x_1^{(i)} = (i-1)w^{(0)}/(N_{\text{nodes}}-1)$, with $i \in \{1, \ldots, N_{\text{nodes}}-1\}$. Along the interval $\left[x_1^{(i)}, x_1^{(i+1)}\right]$ between two nodes, each geometric parameter reads

$$\mathcal{W}^{(n)}(x_1) \coloneqq \sum_{k=0}^{3} a_k \left(d^{(n)} + \frac{w^{(n)}}{2} - x_1^{(i)} \right)^k , \tag{V.3}$$

with a_k the weights of the polynomial interpolation function.

The extreme case of optimizing for a single node implies all parameters will have the same value along $\mathbf{e}_1$ resulting in a zero gradient $\mathbf{e}_1 \cdot \boldsymbol{\nabla}\mathcal{W}^{(n)} = 0$. Using 2 nodes, the possible profiles are affine and linear functions, i.e., they are monotonic and do satisfy $\mathbf{e}_1 \cdot \boldsymbol{\nabla}\mathcal{W}^{(n)} = \text{const.}$ (which implies an asymmetric geometry), but also include the non-graded (constant) cases as sole symmetric profiles. A total of 3 nodes can still provide non-graded and linear profiles, but yields much richer symmetric and non-monotonic profiles. To get a grip on the number of nodes that has to be used, let us consider the following example.

The optimal geometry and far-field directivity of the meta-lens able to steer the acoustic beam by $\theta_{\text{obj}} = +20°$ at frequency $f_{\text{opt}} = 2\,\text{kHz}$ are displayed in Fig. 4. We observe good agreement of the absolute pressure between the analytical model and FEM. Some discrepancies can still be noticed and are linked to the normal velocity profile along Γ_0. The analytical solution of velocity is piece-wise constant while the FEM solution is continuous, and truncation errors in the analytical model also come into play. The results are produced using the PCHIP interpolation with $N_{\text{nodes}} = 3$. The geometry is set with a main duct of height $w^{(0)} = 20\,\text{cm}$, the thickness of the meta-lens is $L = 5\,\text{cm}$, comprising $N = 10$ slits, each of them loaded by $Q = 5$ Helmholtz resonators. The chosen configuration ensures beam deflection, while being relatively easy to manufacture using additive manufacturing methods. The analytical and numerical results are in excellent agreement as presented in Fig. 4**(b)**, showing once again that the proposed explicit model is adapted to the modeling of acoustic meta-lenses for baffled sources.

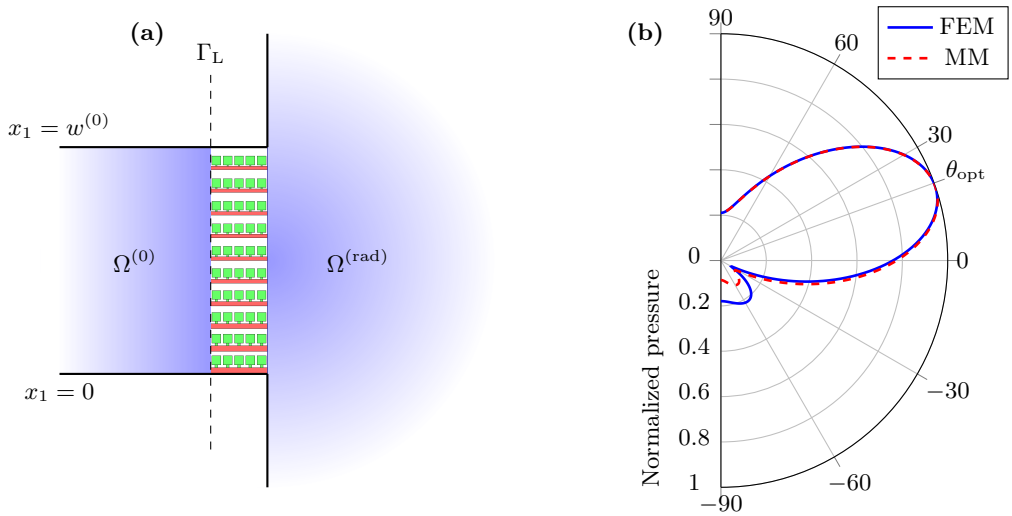

FIG. 4. (Color online) Optimal geometry of the meta-lens for +20° steering at $f_{\text{opt}} = 2\,\text{kHz}$ **(a)**, far-field directivity diagram **(b)** comparing FEM in solid blue and the explicit model in dashed red.

VI. MATERIALS & METHODS

While the FEM results validate the explicit modeling of acoustic meta-lenses, this section focuses on the experimental validation of the results. A sample having the optimal geometry is manufactured and tested in the controlled environment within the anechoic chamber of the Acoustic Laboratory of Le Mans University (LAUM UMR CNRS

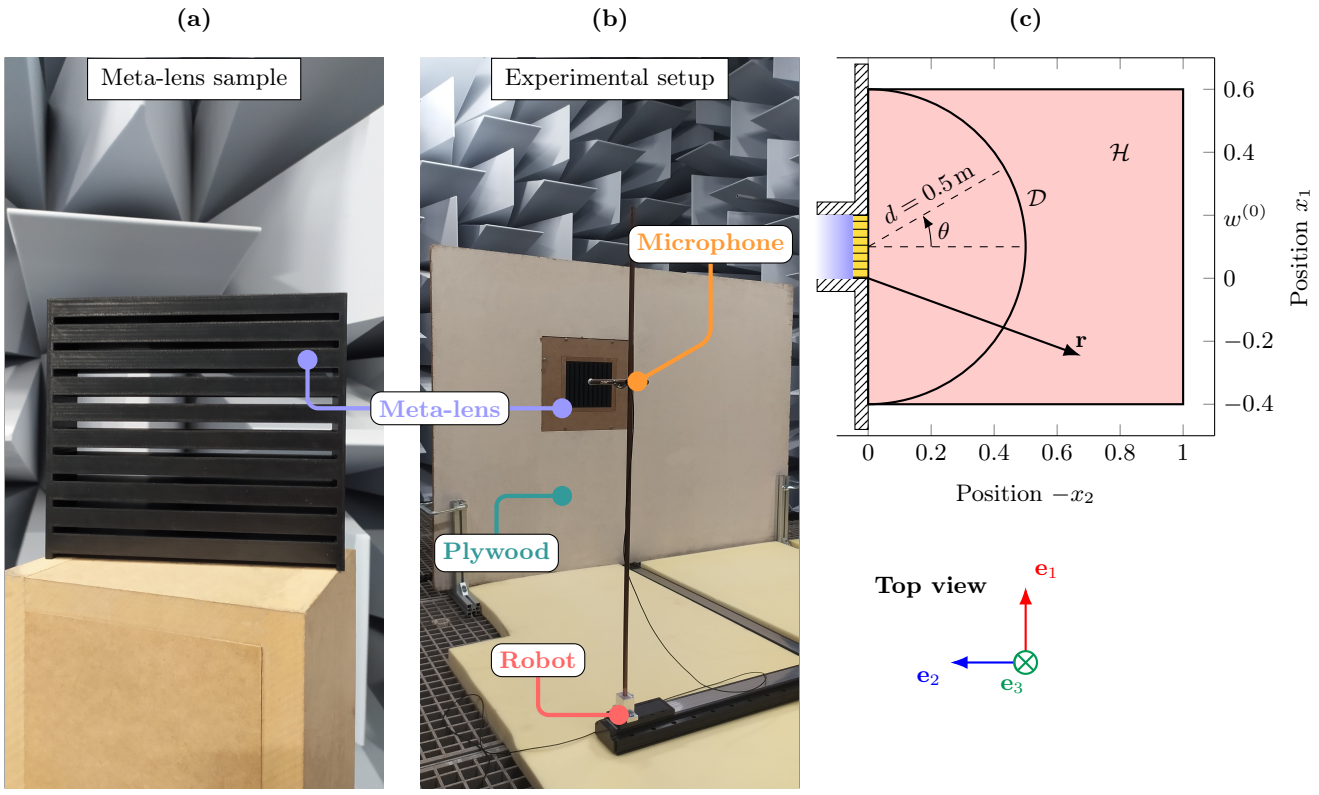

FIG. 5. (Color online) Photography of the sample **(a)** and global view of the experimental setup **(b)**. A sketch of the probed domains is shown in **(c)**.

6613) seen in Fig. 5**(a,b)**. The sample observed in Fig. 5**(a)** is manufactured by Stellantis from a fused-deposition modeling (FDM) process, using the material ABS-M30 on the printer Stratasys Fortus 900mc. The total print time is of approximately 60 hours. The meta-lens is then mounted at the open end of a rectangular duct and baffled by a thick plate of plywood as depicted in Fig. 5**(b)**. On the other end of the duct, 9 square loudspeakers generate a plane wave. The radiated pressure in the anechoic chamber is probed with a microphone.

The source signal is a linear sweep sine between frequencies $f_{\min} = 100\,\mathrm{Hz}$ and $f_{\max} = 3000\,\mathrm{Hz}$. This signal is then amplified with an FX Audio Amplifier HiFi Class D which powers the 9 sources (arranged in a 3-by-3 square array) TEBM36S12-4/A Square BMR® Driver by Tectonic in order to generate a plane wave in the waveguide. The pressure field in the exterior domain is then measured on a 1000 mm × 1000 mm region with a microphone mounted on a moving arm and the results are averaged over 200 cycles. While the analytical model is two-dimensional (meaning that width along $\mathbf{e}_3$ has no importance), the sample has depth $L_3 = w^{(0)} = 20\,\mathrm{cm}$. Hence, the resulting acoustic field is probed on the plane $\mathcal{H}$ as shown in Fig. 5**(b,c)**. The pressure is probed with a 1/4-in. pressure-field microphone (B&K Type 4135) using a pre-amplifier (B&K Type 2670) with signal-conditioning module B&K Nexus. The moving arm is controlled by two linear stages Zaber 001-X-LRT1000AL-E08C, spanning the region $\mathcal{H}$ with an in-plane step $|\Delta\mathbf{x}| = 1\,\mathrm{cm}$. The pressure field is also evaluated along the curve $\mathcal{D}$ at a distance $d = 50\,\mathrm{cm}$ from the center of the meta-lens and over 50 positions on the range $\theta \in [-\pi/2, \pi/2]$.

VII. RESULTS

The results of the two different models as well as the experimental data are presented in this section. First, the profiles of sound speed and refraction angle are shown and evidence the spatially-dependent properties of the meta-lens. Then, the radiated pressure maps and normalized near-field angular response results are presented for the optimized configuration.

A. Sound speed & angle of refraction

In this part, the optimal sound speed and refraction angles are investigated as if the couplings between the slits did not exist. To this purpose, the sound speed within the meta-lens is directly evaluated from the dispersion relation of the unit-cell within each slit. The wavenumber $k^{(n)}$ in the n-th slit satisfies $\cos(k^{(n)}L) = (1/2)\mathrm{Tr}\left(\mathbf{T}^{(n)}\right)$ where Tr is the trace operator. Once calculated, the phase velocity in the slits takes the form $c_\Phi^{(n)} = \omega/\mathrm{Re}\left(k^{(n)}\right)$. In this way the sound speed at the interface Γ_L is given by

$$c_\Phi(x_1) = \begin{cases} c_\Phi^{(n)} & \forall \mathbf{x} \in \Gamma_\mathrm{L}^{(n)}\,, \\ 0 & \forall \mathbf{x} \in \Gamma_\mathrm{L} \backslash \Gamma_\mathrm{L}^{(n)}\,. \end{cases} \tag{VII.1}$$

As the optimal sound speed is piece-wise constant, estimating the refraction angle from Eq. (II.2) has no physical meaning. The derivative $\mathrm{d}(1/c_\Phi)/\mathrm{d}x_1$ is either zero or $\pm\infty$ at the singularities (positions $x_1 = d^{(n)}$ and $x_1 = d^{(n)} + w^{(n)}$). Therefore, the profiles of sound speed and optimal refraction angle are interpolated and shown in Fig. 6.

Another approach is to estimate the profile of sound speed knowing that the refraction angle is $\theta_\mathrm{opt} = +20°$, again using Eq. (II.2). The derivation of the profile is trivial and for a constant refraction angle the sound speed is

$$c_\Phi(x_1) = \left(\frac{x_1}{Lc_0}\sin(\pi/9) + \frac{1}{c_\Phi(0)}\right)^{-1}\,, \tag{VII.2}$$

which is shown by the blue curve in Fig. 6. Both approaches, i.e., computing the sound speed profile for a constant refraction angle and computing the refraction angle from the dispersion relation, give distinct results. On the one hand, we observe what the sound speed profile should be if a constant refraction angle is desired. On the other hand, the effective profile of refraction angle of the meta-lens is retrieved from the dispersion relation of the slits. Additional content is available in Supplementary Material.

B. Radiation & directivity

The meta-lens is optimized for the single frequency $f_\mathrm{opt} = 2\,\mathrm{kHz}$, but experimental results are estimated over $N_\mathrm{f} = 1800$ linearly spaced frequencies within the bounds $f_\mathrm{min} = 1\,\mathrm{kHz}$ and $f_\mathrm{max} = 3\,\mathrm{kHz}$. While the far-field directivity is readily accessible from both the explicit model and FEM, only the near-field acoustic pressure is measured

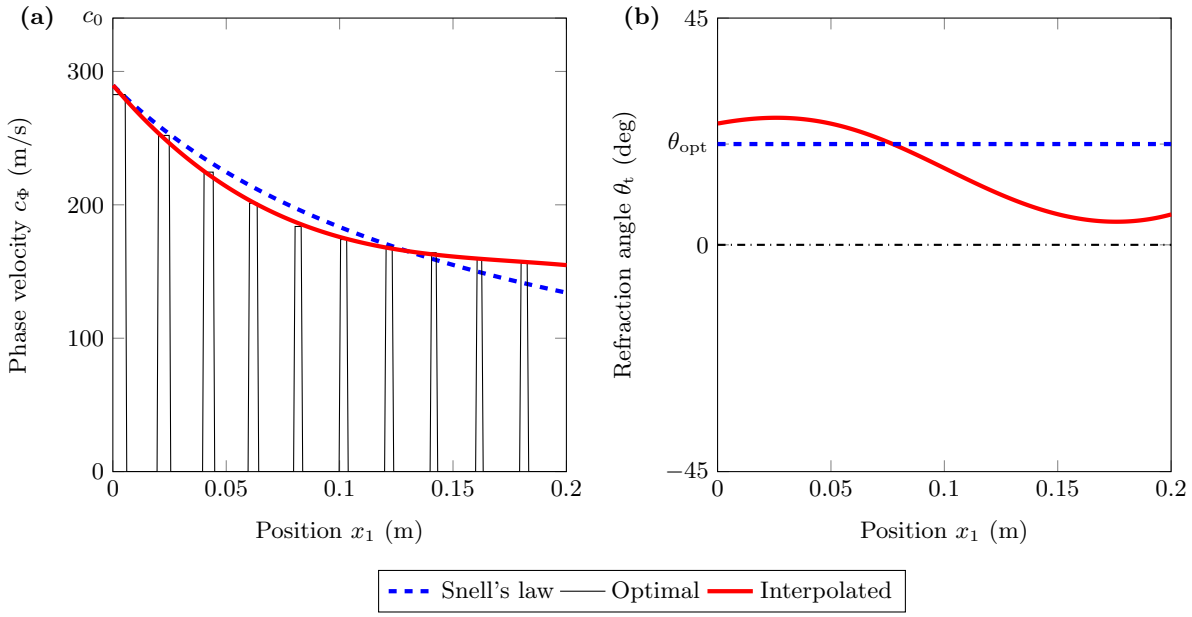

FIG. 6. (Color online) Comparison of optimal sound speeds **(a)** and refraction angles **(b)** according to Snell's law (blue), from the explicit model (black), and interpolated (red).

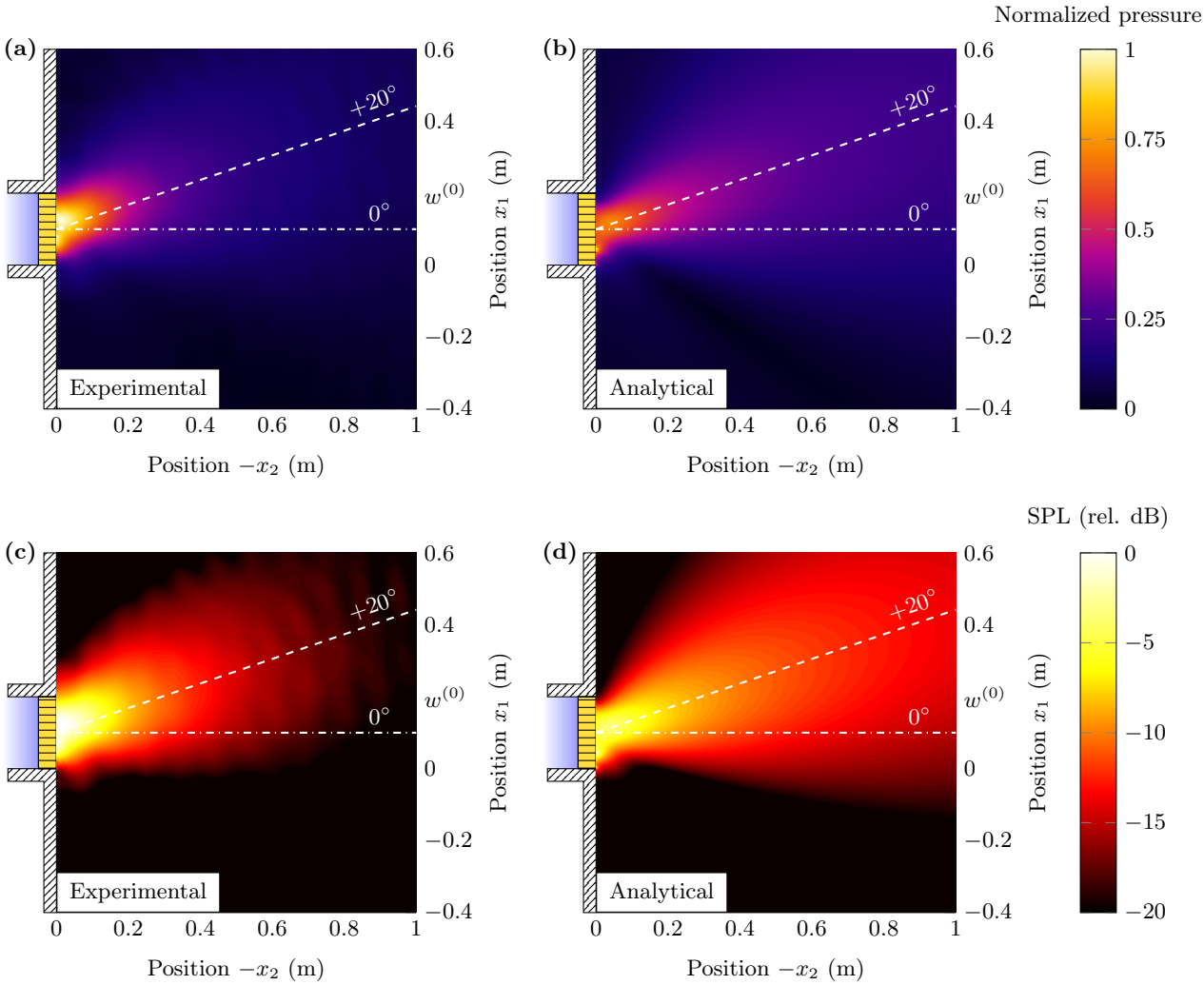

FIG. 7. (Color online) Results for the meta-lens steering the acoustic beam by $\theta_{\text{opt}} = +20°$. Normalized acoustic pressure **(a,b)** and SPL **(c,d)** in the radiated domain $\Omega^{(\text{rad})}$ at frequency $f_{\text{opt}} = 2\,\text{kHz}$. Left panel **(a,c)** shows the experimental results and right panel **(b,d)** the analytical predictions.

experimentally. The results of the radiated acoustic pressure are presented here and the normalized acoustic pressure $|p|/\max|p|$ and SPL are shown in Fig. 7.

We qualitatively observe a good agreement between experimental data and the radiated pressure predicted by the explicit model. However, the acoustic pressure seems to be lower experimentally, which is especially visible on the SPL fields in Fig. 7**(c,d)**. This drop in amplitude is due to the meta-lens being infinite in the explicit model, i.e., the 2D model implies infinite dimension in the out-of-plane direction $\mathbf{e}_3$. In other words, while in the explicit model the pressure at any arbitrary point in $\Omega^{(\text{rad})}$ is the contribution of an infinite source along $\mathbf{e}_3$, this source is only 20 cm-deep in the experiment. Thus, it is expected to experimentally observe a lower pressure amplitude (and a lower SPL) in $\Omega^{(\text{rad})}$. In addition, modes along $\mathbf{e}_3$ are expected to emerge experimentally and located at the same frequencies as those in the $\mathbf{e}_1$ direction because of the waveguide having a square cross-section. This is demonstrated in the Supplementary Material by solving the full 3D problem with FEM.

Besides, part of the incident energy reflected at Γ_{L} then reflected onto the source itself, inevitably altering the incident field in $\Omega^{(0)}$. This effect is presently not accounted for in the present 2D model, but could be a topic of investigation in further studies. Still, the proposed meta-lenses have a high transmission coefficient, which means the part of the incident energy in $\Omega^{(0)}$ which is either absorbed or reflected is relatively low. This translates in the incident field being not significantly disturbed by the high-order reflections between the source and Γ_{L}. In the Supplementary Material, it is shown that the transmission loss is very low, meaning almost the entirety of the incident field goes through the

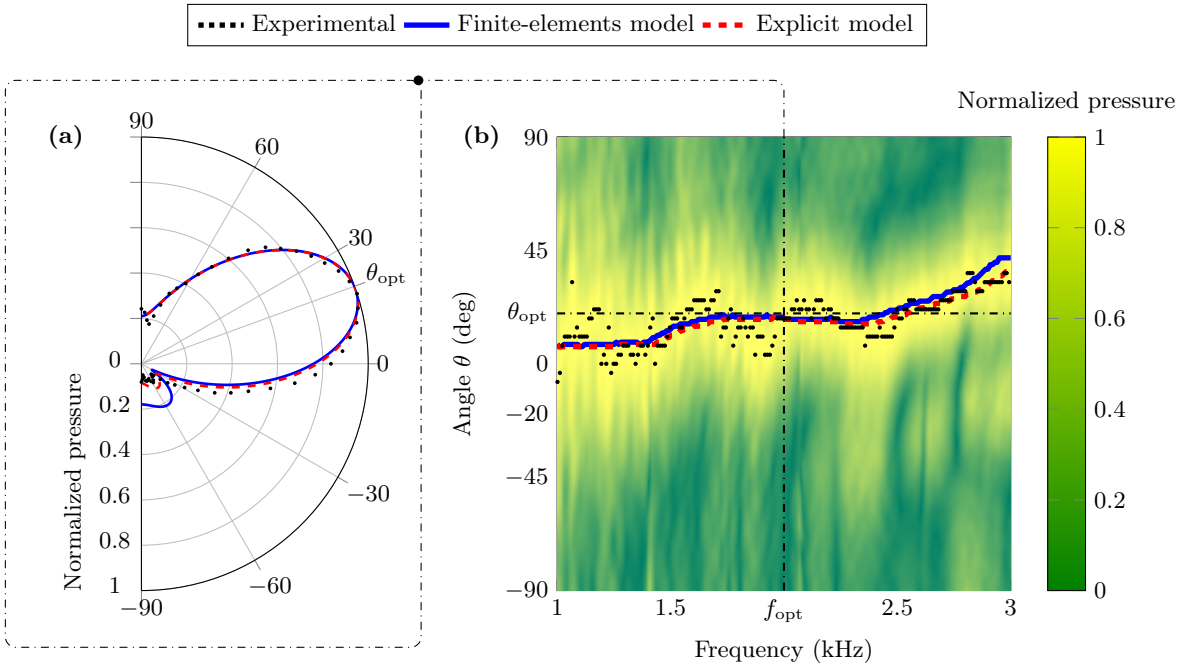

FIG. 8. (Color online) Normalized near-field angular response **(a)** at frequency f_{opt}, and angle of maximal acoustic pressure with respect to frequency **(b)**. Numerical and explicit results in solid blue and dashed red respectively, experimental results in dotted black.

meta-lens. Moreover, the transmission coefficient of the meta-lens could also be maximized and set as an objective function during the optimisation process.

Figure 8**(a)** shows the normalized near-field angular response at the frequency of optimization. Although the meta-lens is optimized for the single frequency f_{opt}, the effect of lensing is preserved across a wider frequency range. This is supported by the results presented in Fig. 8**(b)** over the range $f \in [f_{\text{min}}, f_{\text{max}}]$.

While both FEM and explicit models show a very good agreement, the experimental data is not as smooth, although the general trend is preserved. This is evidenced when superimposing the angle/frequency map of normalized pressure obtained experimentally with the location of the angle of maximal pressure. Here again, this behavior is made possible by the regimes in which the resonant slits are operating and is linked to the configuration of Helmholtz resonators, as evidenced in Supplementary Material.

VIII. CONCLUSIONS

In this work, the behavior of meta-lenses based on slits loaded by Helmholtz resonators is reported mathematically, numerically, and experimentally. The explicit model is developed in two dimensions, accounting for thermal and viscous losses, inter-slit couplings, and high-order modes in the baffled waveguide. In addition, the radiated pressure is estimated semi-analytically via Green's integral formulations. The results of the explicit model are first validated against FEM solutions and both show excellent agreement over multiple configurations and wide frequency ranges, above the cut-off frequency of the main duct.

The explicit model is then used as a kernel for an optimization procedure, providing meta-lenses with optimal geometry for several selected targets, which focus or steer an acoustic beam. A sample having the optimal geometry is built by additive manufacturing and tested experimentally. The experimental results show good agreement with both the FEM and the analytical model, especially for the near-field angular response. While there are discrepancies on the absolute pressure on the experimental observations, which are mainly due to the system being finite and transverse modes, they are accurately predicted by FEM with a 3D geometry.

Although the proposed explicit model has a fair amount of advantages when compared to FEM solutions, limitations still exist. These limitations are mainly related to the truncation of infinite series and integrals, length corrections, and the inter-resonator couplings that may arise in some particular configurations. As previously mentioned, the back-and-forth reflections between the source and the meta-lens are present but can be neglected in case of low

transmission loss.

Finally, the explicit model could be extended in order to account for three-dimensional geometries as the good agreement between the experimental data and 3D FEM simulations is demonstrated. Additionally, the optimization routines could be adapted for multi-frequency cases and further developed for faster minimization times. These improvements would provide an even more robust and complete tool for the modeling and design of acoustic meta-lenses and more generally 3D meta-materials.

ACKNOWLEDGMENTS

This research has been funded by the group Stellantis. J.-P. Groby and V. Romero-García also acknowledge the support of the ANR/RGC METARoom project (ANR-18-CE08-002).

CREDIT AUTHORSHIP CONTRIBUTION STATEMENT

Théo Cavalieri: Methodology, Software, Validation, Formal analysis, Investigation, Resources, Data Curation, Writing - Original Draft, Writing - Review & Editing, Visualization. **Vicent Romero-García:** Conceptualization, Methodology, Validation, Formal analysis, Investigation, Resources, Data Curation, Writing - Review & Editing, Supervision. **Manuel Melon:** Conceptualization, Methodology, Validation, Formal analysis, Investigation, Resources, Writing - Review & Editing, Supervision, Project administration, Funding acquisition. **Jean-Christophe Chamard:** Conceptualization, Resources, Supervision, Project administration. **Jean-Philippe Groby:** Conceptualization, Methodology, Validation, Formal analysis, Investigation, Resources, Data Curation, Writing - Review & Editing, Supervision.

DATA AVAILABILITY

The data that support the findings of this study are available in the Supplementary Material.

[1] M. Amin, O. Siddiqui, M. Farhat, and A. Khelif. A perfect Fresnel acoustic reflector implemented by a Fano-resonant metascreen. *J. Appl. Phys.*, 123(14):144502 (2018).
[2] M. Amin, O. Siddiqui, W. Orfali, M. Farhat, and A. Khelif. Resonant Beam Steering and Carpet Cloaking Using an Acoustic Transformational Metascreen. *Phys. Rev. Appl.*, 10(6):064030 (2018).
[3] P. Benner, A. Cohen, M. Ohlberger, and K. Willcox, editors. *Model reduction and approximation: theory and algorithms*. SIAM J. Appl., Philadelphia, 2017.
[4] J.-P. Berenger. A perfectly matched layer for the absorption of electromagnetic waves. *J. Comput. Phys.*, 114(2):185–200 (1994).
[5] T. Betlehem, W. Zhang, M. A. Poletti, and T. D. Abhayapala. Personal Sound Zones: Delivering interface-free audio to multiple listeners. *IEEE Signal Processing Magazine*, 32(2):81–91 (2015).
[6] F. Bloch. Ueber die Quantenmechanik der Elektronen in Kristallgittern. *Zeitschrift fuer Physik*, 52(7-8):555–600, 1929.
[7] M. Born and E. Wolf. *Principles of optics*. Cambridge University Press, Cambridge, United Kingdom, 2019.
[8] B. Brouard, D. Lafarge, and J.-F. Allard. A general method of modelling sound propagation in layered media. *J. Sound Vib.*, 183(1):129–142 (1995).
[9] M. Bruneau. *Fundamentals of acoustics*. ISTE Ltd, 2006.
[10] C. Kai C., K. F. Leong, and C. S. Lim. *Rapid prototyping: principles and applications*. World Scientific, New Jersey, 2nd edition, 2003.
[11] V. Dubos, A. Khettabi, D. H. Keefe, C. J. Nederveen, and AC. Pijnacker. Theory of Sound Propagation in a Duct with a Branched Tube Using Modal Decomposition. *Acta Acust*, 85:18 (1999).
[12] S. J. Elliott and M. Jones. An active headrest for personal audio. *J. Acoust. Soc. Am.*, 119(5):2702–2709 (2006).
[13] F. N. Fritsch and R. E. Carlson. Monotone Piecewise Cubic Interpolation. *SIAM J. Numer. Anal.*, 17(2):238–246, 1980.
[14] T. Grimm. *User's guide to rapid prototyping*. SME, Dearborn, Mich, 2004.
[15] J.-P. Groby, W. Huang, A. Lardeau, and Y. Aurégan. The use of slow waves to design simple sound absorbing materials. *J. Appl. Phys.*, 117(12):124903 (2015).
[16] J.-P. Groby, R. Pommier, and Y. Aurégan. Use of slow sound to design perfect and broadband passive sound absorbing materials. *J. Acoust. Soc. Am.*, 139(4):1660–1671 (2016).

[17] J.-P. Groby. *Modélisation de la propagation des ondes élastiques générées par un séisme proche ou éloigné à l'intérieur d'une ville*. PhD thesis, Université de la Méditerranée - Aix-Marseille II, Marseille, 2005.

[18] R. A. Horn and C. R. Johnson. *Matrix analysis*. Cambridge University Press, New York, NY, 2nd edition, 2017.

[19] J. Kennedy and R. Eberhart. Particle swarm optimization. In *Proceedings of ICNN'95 - International Conference on Neural Networks*, volume 4, pages 1942–1948, Perth, WA, Australia, 1995

[20] J. Kergomard and A. Garcia. Simple discontinuities in acoustic waveguides at low frequencies: Critical analysis and formulae. *J. Sound. Vib.*, 114(3):465–479 (1987).

[21] J. Lan, Y. Li, Y. Xu, and X. Liu. Manipulation of acoustic wavefront by gradient metasurface based on Helmholtz Resonators. *Sci. Rep.*, 7(1):10587 (2017).

[22] Y. Li, S. Qi, and M Badreddine Assouar. Theory of metascreen-based acoustic passive phased array. *New J. Phys.*, 18(4):043024 (2016).

[23] X. Liao, J. Cheer, S. Elliott, and S. Zheng. Design of a Loudspeaker Array for Personal Audio in a Car Cabin. *J. Audio Eng. Soc.*, 65(3):226–238 (2017).

[24] J. A. Nelder and R. Mead. A Simplex Method for Function Minimization. *Comput J*, 7(4):308–313 (1965).

[25] M. C. Pease. *Methods of Matrix Algebra*. Elsevier NetLibrary, Incorporated, New York, Boulder, 1965.

[26] M.E.H. Pedersen and A.J. Chipperfield. Simplifying Particle Swarm Optimization. *Appl. Soft Comput.*, 10(2):618–628 (2010).

[27] W. H. Press. *Numerical recipes: the art of scientific computing*. Cambridge University Press, Cambridge, UK ; New York, 3rd ed edition, 2007.

[28] V. Romero-García, N. Jiménez, J.-P. Groby, A. Merkel, V. Tournat, G. Theocharis, O. Richoux, and V. Pagneux. Perfect Absorption in Mirror-Symmetric Acoustic Metascreens. *Phys. Rev. Appl.*, 14(5):054055 (2020).

[29] S. H Schot. Eighty years of Sommerfeld's radiation condition. *Hist. Math.*, 19(4):385–401 (1992).

[30] A. Sommerfeld. *Partial differential equations in physics*. Lectures on theoretical physics. Acad. Pr, New York, 1964.

[31] M. R. Stinson. The propagation of plane sound waves in narrow and wide circular tubes, and generalization to uniform tubes of arbitrary cross-sectional shape. *J. Acoust. Soc. Am*, 89(2):550–558 (1991).

[32] A. N. Stroh. Steady State Problems in Anisotropic Elasticity. *J. Math. Phys.*, 41(1-4):77–103 (1962).

[33] L. Vindrola, M. Melon, J.-C. Chamard, and B. Gazengel. Use of the filtered-x least-mean-squares algorithm to adapt personal sound zones in a car cabin. *J. Acoust. Soc. Am.*, 150(3):1779–1793 (2021).

[34] E. G. Williams. *Fourier acoustics: sound radiation and nearfield acoustical holography*. Acad. Pr, San Diego, Calif, 1999.

[35] Y. Xie, W. Wang, H. Chen, A. Konneker, B.-Ioan Popa, and S. A. Cummer. Wavefront modulation and subwavelength diffractive acoustics with an acoustic metasurface. *Nat. Commun.*, 5(1):5553 (2014).

[36] See Supplemental Material at http://link.aps.org/supplemental/XXXXXX for more details on the calculations.